Application of Pattern Recognition Techniques for Classification of Pediatric Brain Tumors by In Vivo 3T [1]H-MR Spectroscopy—A Multi-Center Study

Niloufar Zarinabad [ID],[1,2] Laurence J. Abernethy,[3] Shivaram Avula,[3]
Nigel P. Davies,[1,2,4] Daniel Rodriguez Gutierrez,[5,6] Tim Jaspan,[5,7]
Lesley MacPherson,[2] Dipayan Mitra,[8] Heather E.L. Rose,[1,2] Martin Wilson,[9]
Paul S. Morgan,[5,6,10] Simon Bailey,[11] Barry Pizer,[12] Theodoros N. Arvanitis,[2,13]
Richard G. Grundy,[5] Dorothee P. Auer,[5,7,10] and Andrew Peet[1,2]*

Purpose: 3T magnetic resonance scanners have boosted clinical application of ^{1}H-MR spectroscopy (MRS) by offering an improved signal-to-noise ratio and increased spectral resolution, thereby identifying more metabolites and extending the range of metabolic information. Spectroscopic data from clinical 1.5T MR scanners has been shown to discriminate between pediatric brain tumors by applying machine learning techniques to further aid diagnosis. The purpose of this multi-center study was to investigate the discriminative potential of metabolite profiles obtained from 3T scanners in classifying pediatric brain tumors.

Methods: A total of 41 pediatric patients with brain tumors (17 medulloblastomas, 20 pilocytic astrocytomas, and 4 ependymomas) were scanned across four different hospitals. Raw spectroscopy data were processed using TARQUIN. Borderline synthetic minority oversampling technique was used to correct for the data skewness. Different classifiers were trained using linear discriminative analysis, support vector machine, and random forest techniques.

Results: Support vector machine had the highest balanced accuracy for discriminating the three tumor types. The balanced accuracy achieved was higher than the balanced accuracy previously reported for similar multi-center dataset from 1.5T magnets with echo time 20 to 32 ms alone.

Conclusion: This study showed that 3T MRS can detect key differences in metabolite profiles for the main types of childhood tumors. **Magn Reson Med 79:2359–2366, 2018. © 2017 The Authors Magnetic Resonance in Medicine published by Wiley Periodicals, Inc. on behalf of International Society for Magnetic Resonance in Medicine. This is an open access article under the terms of the Creative Commons Attribution License, which permits use, distribution and reproduction in any medium, provided the original work is properly cited.**

Key words: MR spectroscopy; 3T; pediatric brain tumors; diagnosis; classification

[1]Institute of Cancer and Genomics Sciences, University of Birmingham, Birmingham, United Kingdom.

[2]Birmingham Children's Hospital, Birmingham, United Kingdom.

[3]Department of Radiology, Alder Hey Children's NHS Foundation Trust, Liverpool, United Kingdom.

[4]Department of Imaging and Medical Physics, University Hospitals Birmingham NHS Foundation Trust, Birmingham, United Kingdom.

[5]The Children's Brain Tumour Research Centre, University of Nottingham, Nottingham, United Kingdom.

[6]Medical Physics, Nottingham University Hospital, Queen's Medical Centre, Nottingham, United Kingdom.

[7]Neuroradiology, Nottingham University Hospital, Queen's Medical Centre, Nottingham, United Kingdom.

[8]Neuroradiology Department, Newcastle upon Tyne Hospitals, Newcastle upon Tyne, United Kingdom.

[9]Centre for Human Brain Health, School of Psychology, University of Birmingham, Birmingham, United Kingdom.

[10]Radiological Sciences, Department of Clinical Neuroscience, University of Nottingham, Nottingham, United Kingdom.

[11]Paediatric Oncology Department, Great North Children's Hospital, Newcastle upon Tyne, United Kingdom.

[12]Department of Paediatric Oncology, Alder Hey Children's NHS Foundation Trust, Liverpool, United Kingdom.

[13]Institute of Digital Healthcare, WMG, University of Warwick, Coventry, United Kingdom.

*Correspondence to: Andrew Peet, F.R.C.P.C.H., Ph.D., Institute of Child Health, Whittall Street, Birmingham B4 6NH, United Kingdom. Tel: 0121-333-8234; Fax: 0121-333-8241; E-mail: a.peet@bham.ac.uk; Twitter: @bhambtrg

INTRODUCTION

Brain tumors are a significant cause of death and long-term disability in children, with a range of treatment options and outcomes depending on the tumor type, location, and age of the patient. Histopathology following biopsy or surgical resection is the current gold standard for diagnosis of brain tumor type and grade (1). Although surgical resection is often appropriate for many tumors and also provides a histological diagnosis, there are distinct advantages to having a diagnosis before surgery. A pre-operative diagnosis can influence the extent of surgical resection attempted, allow the timely planning of adjuvant treatment and aid discussions with the family. Conventional magnetic resonance imaging (MRI) is commonly used to propose a diagnosis before surgery but is of limited accuracy. A previous study reviewed the radiological reports from a cohort of children

with medulloblastoma, pilocytic astrocytoma, or ependymoma and showed an accuracy of diagnosis of 66% (2).

MRI techniques have significantly advanced in recent years with new imaging techniques being able to provide information on tissue properties, structure, and basic metabolic processes. Amongst these new techniques, ^{1}H-MR spectroscopy (MRS) has the ability to provide non-invasive measurements of metabolite profiles with the potential to aid diagnosis and improve the characterization of pediatric brain tumors (3–8).

Spectroscopic studies on pediatric brain tumors have attempted to characterize different histologic types and predict the degree of malignancy (7,9). Non-invasive grading is especially important for tumors in the eloquent areas or deeply located tumors. Single and multi-center studies have worked on development and optimization of diagnostic classifiers of childhood brain tumors using MRS. This has yielded promising results in discriminating between certain common tumor types (6,7).

With the integration of 3T MRI into clinical practice, there is growing interest in the practical improvement of MRS at a 3T field strength over the more established magnetic field strength of 1.5T, because both the spectral resolution and the spatial resolution depend, in a linear fashion, on the magnetic field (10–12).

Although single-voxel MRS of the human brain has been carried out at many field strengths (from 0.5T to 7T), to date, no study has been reported on application of pattern recognition techniques for classification of pediatric brain tumors using 3T MRS.

The aim of this study was to evaluate the discriminative potential of metabolites obtained from 3T MRI scanners in classifying pediatric brain tumors by comparing the performance of three different pattern recognition techniques.

METHODS

Patients

This study included 52 patients less than 16 years of age (8.2 ± 5.32 years, 21 female and 31 male) with histologically proven brain tumor collected from four centers in the United Kingdom. Patient data were collected retrospectively from children who underwent single-voxel MRS between November 2009 and April 2016 during a routine MRI for a suspected brain tumor before treatment.

The enrolled cohort consisted of patients with three different tumor types from all regions of the brain, including medulloblastoma (MB) ($n = 18$), pilocytic astrocytoma (PA) ($n = 26$), and ependymoma (EP) ($n = 8$). Histopathological, clinical, and radiological features were used to form a diagnosis agreed by a multidisciplinary team. Approval was obtained from the research ethics committee and informed consent given by parents/guardians.

Data Acquisition

All studies were performed using 3T scanners from different manufacturers (Philips Achieva, Siemens MAGNETOM Verio). MRS was performed after conventional MRI that included T_1- and T_2-weighted and T_1-weighted post-contrast sequences. Spectroscopy images were acquired using a point resolved single voxel spectroscopy (PRESS) sequence (time echo = 30–46 ms, pulse repetition time = 2000 ms). Cubic voxels size varied from $3.38\,cm^3$ to $8\,cm^3$ and 128 repetitions were used. A water unsuppressed acquisition was also acquired as a concentration reference. Conventional MRI was used for guiding voxel placement to ensure it is entirely located within the tumor

MRS Processing

Raw spectroscopy data were processed using TARQUIN (version 4.3.6) (13) fitting to a linear combination of 19 metabolite basis functions generated at the correct field strength and echo time with an additional 9 lipid and macromolecular components (13–15). Frequency alignment, zero order phase correction, baseline correction, and water removal using Hankel singular value decomposition (HSVD) methods were applied by TARQUIN. TARQUIN determines the chemical shift offset, phase, and baseline during the fitting process. It then zero fills the time domain data by a factor of 2 ($\times 2$) and converts the time domain signal to spectral domain using a Fourier transform. The obtained spectra are then resampled to 0.49 Hz/point. This is to ensure all cases have a consistent Hz/point. The resampled spectra are used for analysis in this study. The full spectral range (−3.00 to 12.5 ppm) was used for fitting the data and metabolite quantitation. Quantitation was carried out relative to a water reference spectrum. Corrections for T_2 relaxation times of metabolites and water were applied as the default values for TARQUIN (16). To include the metabolites of interest in the study, main metabolites in 0.5 to 4 ppm region were used for classification.

Out of 52 enrolled cases, 41 cases (medulloblastoma $n = 17$, pilocytic astrocytoma $n = 20$, and ependymoma $n = 4$, of which 1 is analplastic ependymoma) passed the following quality control criteria: signal-to-noise ratio obtained from TARQUIN (SNR)≥ 4 (here SNR is defined as ratio between the maximum in the spectrum minus baseline divided by $2 \times$ root-mean-square of the spectral noise level), full-width half-maximum obtained from TARQUIN (FWHM)≤ 0.15 ppm, stable baseline, good phasing, adequate water suppression, and absence of artefacts. The voxel position was also reviewed to ensure it was positioned over tumor, did not include significant amounts of normal-appearing brain or cyst, and was at least 3 mm away from lipid-containing bone and scalp. The 11 failed cases include medulloblastoma $n = 1$, pilocytic astrocytoma $n = 6$, and ependymoma $n = 4$. A poor voxel placement that included normal brain, small voxel size, and low quality spectra were the main quality control failure reasons for the latter cases.

For the quantified metabolite profiles, Crammer-Rao lower bounds were calculated to evaluate metabolite accuracy. All metabolites where at least two patients had a Crammer-Rao lower bound < 50 were included (alanine, aspartate and GABA were excluded) (7). The following metabolites were used for classification: citrate (Cit), glucose (Glc), glutamine (Gln), glutathione (Glth), glutamate (Glu), glycine (Gly), myo-inositol (mIns), lactate (Lac), total choline (tCho = glycerophosphocholine [GPC] + phosphocholine [PCh]), scyllo-inositol (scyllo), taurine (Tau), total creatine (tCr = Cr + PCr), and total NAA (tNAA = NAA + NAAG). The nine macromolecular and lipid components were grouped together to account for three broad resonances at

Table 1
Estimated Metabolite Concentration ± SD Calculated by TARQUIN[a].

Metabolite	Ependymoma (n = 4)	Medulloblastoma (n = 17)	Pilocytic Astrocytoma (n = 20)	P-Value
Cit*	0.96 ± 0.21	0.56 ± 0.31	0.47 ± 0.48	0.031
Glc	1.2 ± 0.27	2.3 ± 1.7	1.07 ± 1.06	0.073
Gln	1.69 ± 0.11	2.6 ± 1.53	2.2 ± 2.6	0.429
Glth*	1.12 ± 0.32	1.8 ± 0.8	0.66 ± 0.6	<0.000
Glu	1.14 ± 0.94	2.4 ± 2.2	3.2 ± 2.3	0.055
Gly*	1.92 ± 0.5	3.7 ± 2.08	0.73 ± 0.76	<0.000
mIns	4.53 ± 2.3	2.29 ± 1.66	1.94 ± 1.73	0.097
Lac*	1.39 ± 0.68	1.65 ± 1.7	0.65 ± 0.74	0.041
Scyllo*	0.008 ± 0.01	0.37 ± 0.47	0.05 ± 0.08	0.009
Tau*	0.6 ± 0.75	6.3 ± 4.1	1.07 ± 1.03	<0.000
tNAA* (tNAA = NAA + NAAG)	0.53 ± 0.25	1.03 ± 0.44	1.37 ± 0.95	0.007
tCho*	1.69 ± 0.29	3.94 ± 1.74	1.4 ± 0.709	<0.000
tCr*	1.69 ± 0.79	3.91 ± 1.5	2.29 ± 2.22	0.003
tLM09	3.7 ± 1.4	4.94 ± 2.4	3.02 ± 1.87	0.084
tLM13*	21.4 ± 10.05	19.32 ± 13.01	7.8 ± 3.7	<0.000
tLM20	7.2 ± 1.8	7.53 ± 4.1	6.3 ± 3.4	0.444

Cit, citrate; Glc, glucose; Gln, glutamine; Glth, glutathione; Glu, glutamate; Gly, glycine; Lac, lactate; mIns, myo-inositol; NAA,N-acetylaspartate; NAAG,N-Acetylaspartylglutamic acid; scyllo, scyllo-inositol; SD, standard deviation; Tau, taurine; tNAA, total N-acetylaspartate; tCho, total cho-line; tCr, total creatine; tLM09, lipids and macromolecules 0.9; tLM13, lipids and macromolecules 1.3; tLM20, lipids and macromolecules 2.0.
[a]The P-value of analysis of variance (calculated using Kruskal-Wallis test with α = 0.05) is comparing ependymoma versus medullobas-toma versus pilocytic astrocytoma.
*Metabolites with P-values less than 0.05.

0.9 ppm (tLM09), 1.3 ppm (tLM13), and 2.0 ppm (tLM20), giving a maximum of 16 variables.

The Kruskal-Wallis test for the analysis of variance (α = 0.05) was applied to determine the significant differences in metabolite concentrations between the three groups. Mann-Whitney U tests were carried out to compare mean metabolite values between individual pair of groups. Statistical analysis was carried out using SPSS statistics software (version 21.0).

Classification

Borderline synthetic minority oversampling technique (bSMOTE) (17) was used to overpopulate the original ependymoma group by 100% and correct for the skew-ness and class imbalance in the original data. Over-sampled ependymoma was added to the original data sets to create an overpopulated metabolite feature set. Princi-pal component analysis was used to reduce dimension of this overpopulated set and extract features that best dis-criminate between the three tumor groups.

Classifiers were trained using linear discriminative analysis (LDA), support vector machine (SVM), and ran-dom forest (RF) approaches. These techniques have low, medium, and high model flexibility, respectively. A radial basis (Gaussian) function kernel was chosen for SVM. LDA was trained using diagonal linear learner where all classes have the same diagonal covariance matrix.

Developed classifiers using the bSMOTE-overpopulated sets were tested using the original data and the validity of the classifier was checked by comparison with the known histological assignment. Ten-fold cross-validation was used to evaluate the learning algorithm performance. To evaluate classifiers trained using bSMOTE data, the origi-nal data set is partitioned into $z = 10$ pools in which one pool is used for evaluation while the remaining $z - 1$ pools are added to the bSMOTE ependymoma cases, obtained from oversampling ependymoma cases in the remaining $z - 1$ pools, and used for training to produce mean error rates, where $z \in \{1, 2, \ldots, Z\}$. The pools were then ran-domly rotated and the subsampling and permutation tests were repeated until all pools had been evaluated exactly

Table 2
Differentiation between Tumor Metabolite Profiles at 3T Comparing Those that Are Often Included in Differential Diagnoses on Conventional Radiology Using Mann-Whitney U-Test With P-Values Reported.

	Ependymoma (n = 4)	Pilocytic Astrocytoma (n = 20)
Medulloblastoma (n = 17)	↓ Cit*	↑ Glc**
	↑ tCho**	↑ Glth***
	↑ tCr**	↑ Gly***
	↑ Tau**	↑ Lac*
	↓ mIns*	↑ Tau***
		↑ tCho**
		↑ tCr**
		↑ scyllo**
		↑ tLM09*
		↑ tLM13***
	Ependymoma (n = 4)	
Pilocytic astrocytoma (n = 20)	↓ Cit*	
	↑ Glu*	
	↓ Gly**	
	↑ tNAA**	
	↓ tML13*	
	↓ mIns*	

Cit, citrate; Glc, glucose; Glth, glutathione; Glu, glutamate; Gly, glycine; Lac, lactate; mIns, myo-inositol; scyllo, scyllo-inositol; Tau, taurine; tNAA, total N-acetylaspartate; tCho, total choline; tCr, total creatine; tLM 09, lipids and macromolecules 0.9; tLM 13, lipids and macromolecules 1.3.
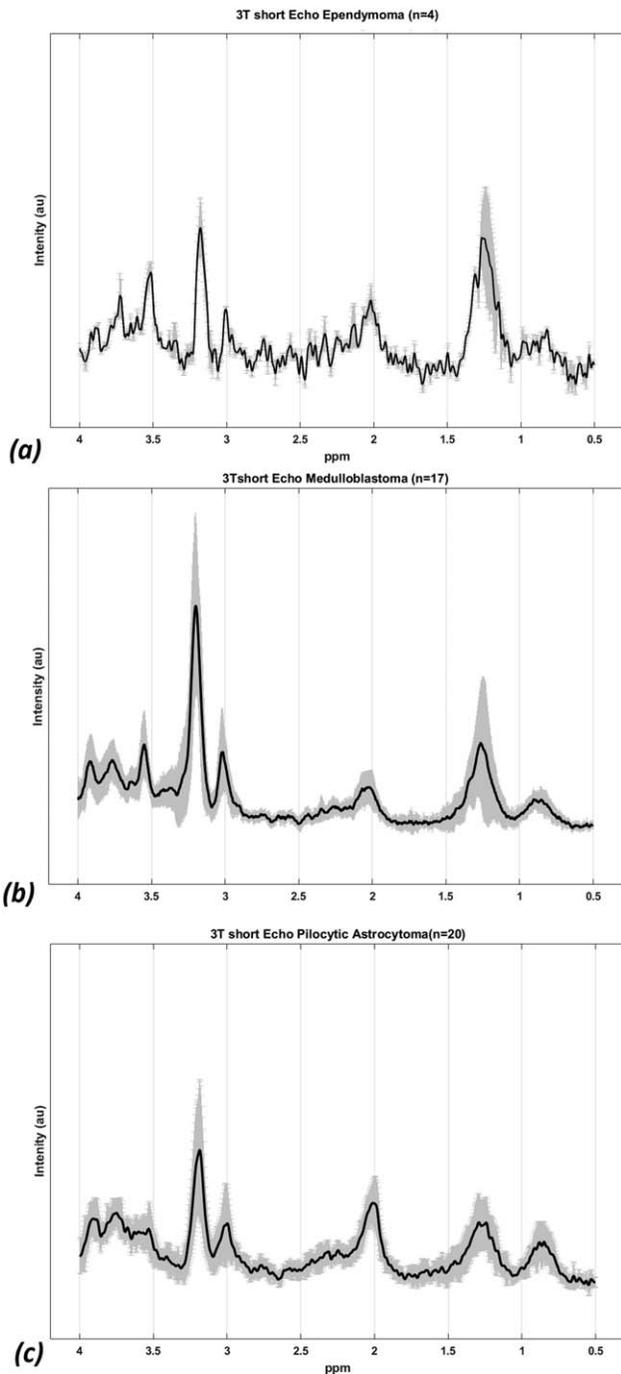*P ≤ 0.05; **P < 0.01; ***P < 0.001.

FIG. 1. Mean 3T short time echo spectra for (**a**) ependymoma (*n* = 4), (**b**) medulloblastoma (*n* = 17), and (**c**) pilocytic astrocytoma (*n* = 20) with solid black line indicating the mean spectra and SD indicated by the shaded region.

once. This ensured that there were no bSMOTE ependymoma cases in any of the test sets. The analysis have been repeated 100 times and results been averaged.

G-mean and F-measure metrics were used for more precise performance evaluation in class imbalance learning. The balanced accuracy rate (BAR) of the learning algorithm, calculated as the mean of the accuracies for the three tumor types, is also reported here as a performance measure metric. In this study, all learning algorithms were developed in python 2.7 (Python

Software Foundation, Wilmington, DE) using Scikit-learn (Version 0.16.1) and Orange (Version 2.6a2) libraries.

RESULTS

Mean metabolite concentrations (mM) ± standard deviations (SD) for each diagnostic group are represented in Table 1. Analysis of variance revealed significant differences between ependymoma, pilocytic astrocytoma, and medulloblastoma in ten of the individual metabolites and combined macromolecules and lipids at 1.3 ppm. Glc, Gln, Glu, mIns, tLM09, and tLM20 had *P*-values > 0.05. Results comparing metabolites between specific pairs of tumor types are reported in Table 2. MB demonstrated increased Tau and decreased mIns compared to EP. Compared with PA, MB had a number of significantly higher metabolites including tCho, Tau, scyllo, tCr, Gly, Glth, and tLM1.3. Compared with EP, PA demonstrated elevated tNAA and decreased tLM13 and mIns. Mean MRS spectra of the three tumor types is presented in Figure 1.

Principal component analysis was carried out and principal components accounting for 95% of variance were extracted, giving four principal components. Figure 2 shows the three-dimensional scatter plot of the three tumor groups using the first three principal components. Data points of each tumor types demonstrated a good degree of data clustering and separation. The four principal components were then submitted to SVM, RF, and LDA learning algorithms and classifiers were compared in view of their performance.

The bar plot in Figure 3 characterizes PCA loadings of the metabolite set for the four main components. tLM13 has dominated the first principal component. Except Glu and tNAA, all loadings on the first principal component are positive. tLM20, Tau, Gly, tCho, and tCr were highly loaded on the second principal component. For the third principal component, Glc, Glu, mIns, tLM20, and Tau with a negative load were the most dominant. In the fourth principal component, the majority of the
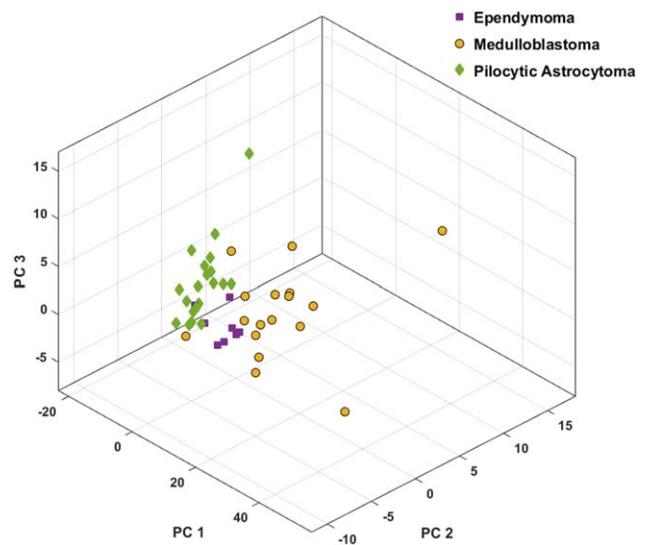

FIG. 2. 3D scatter plot presents principal component analysis (PCA) space for the discrimination of medulloblastoma (MB), pilocytic astrocytoma (PA), and ependymoma (EP).
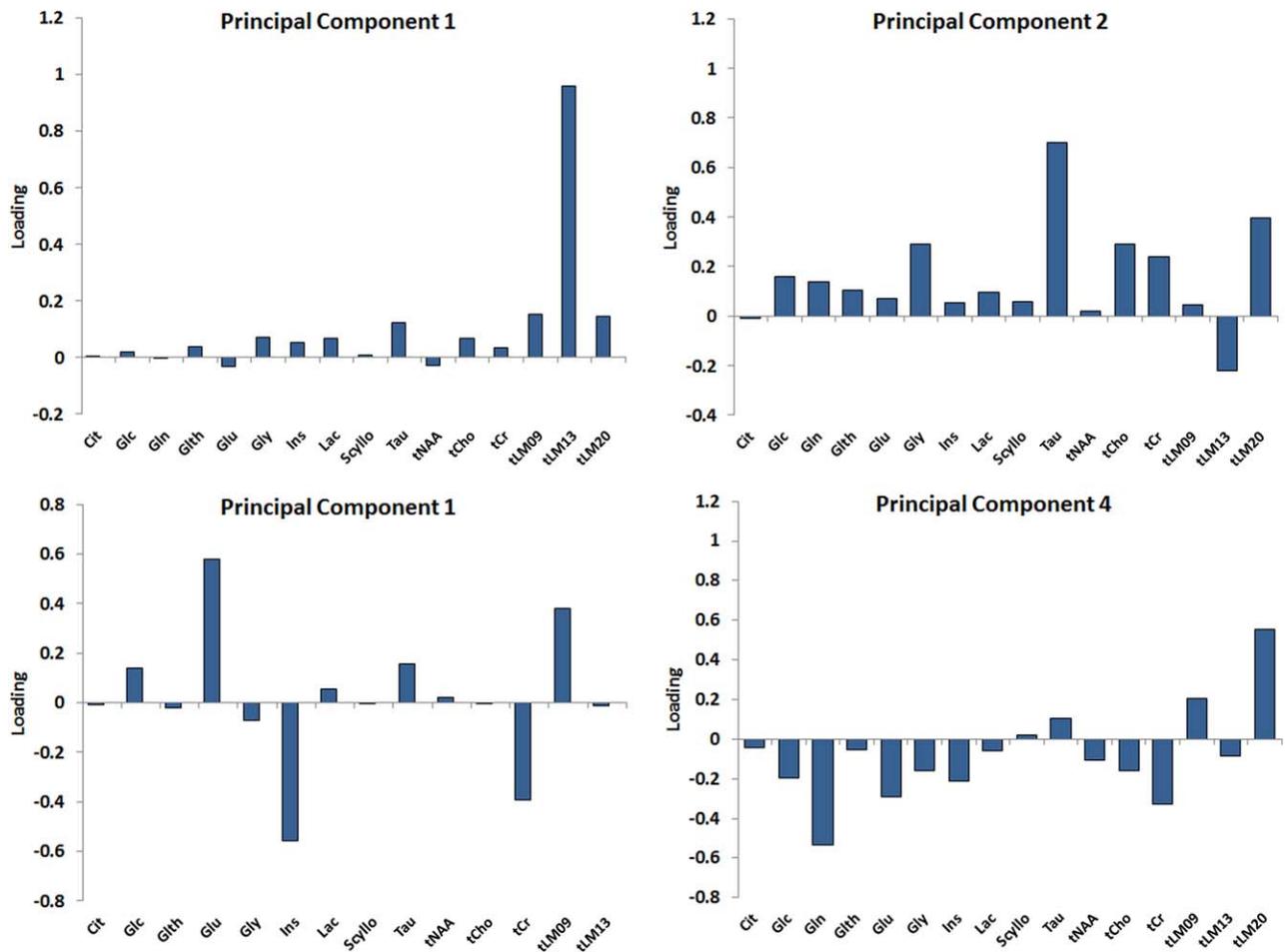
FIG. 3. The Bar plot represents the PCA loadings of the metabolite sets for the main principal components demonstrating how the principal components are loaded with the metabolites features.

metabolites were negatively loaded, however, except Gln, they all were <0.4.

BAR of the learning algorithms and their corresponding individual tumor types, F-measure and G-mean, are presented in Table 3. SVM (BAR = 0.86) performed favorably in comparison to RF (BAR = 0.84) and LDA (BAR = 0.81) in discriminating between the three tumor types. Figure 4 represents the BAR for the three pattern-recognition techniques with their accuracy in discriminating individual tumor groups. To further evaluate and describe the differences between the three learning algorithms performance, analysis of variance was carried out

on the BAR data obtained from 100 runs of samplings. The three methods showed to have BAR mean of significantly different from each other ($P < 0.0001$) (Fig. 5). RF had higher variance ($\sigma^2 = 0.002$) in comparison to the LDA ($\sigma^2 = 0.0016$) and SVM ($\sigma^2 = 0.0011$).

Comparing methods in view of their performance in classifying EP, all methods had similar accuracy (EP accuracy = 0.75) and misclassified one case as PA.

Table 3
Balanced Accuracy Rate (BAR) of the Pattern Recognition Techniques along With Individual Tumor Type F-Measure and G-Mean.

| | | F | | | G-Mean | |
	BAR	EP	MB	PA	EP	MB	PA
LDA	0.81	0.54	0.82	0.9	0.52	0.84	0.91
SVM	0.86	0.85	0.9	0.9	0.86	0.9	0.9
RF	0.84	0.75	0.9	0.87	0.76	0.84	0.87

LDA, linear discriminate analysis; RF, Random forest; SVM, support vector machine; MB, medulloblastoma; PA, pilocytic astrocytoma; EP ependymoma.
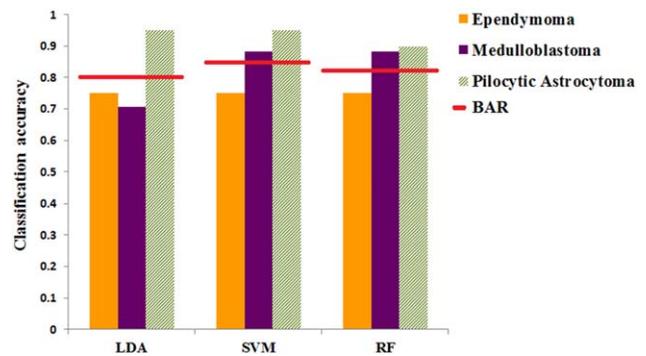

FIG. 4. Bar plots represent individual tumor group classification accuracy along with their balanced accuracy comparing performance of the pattern recognition techniques.
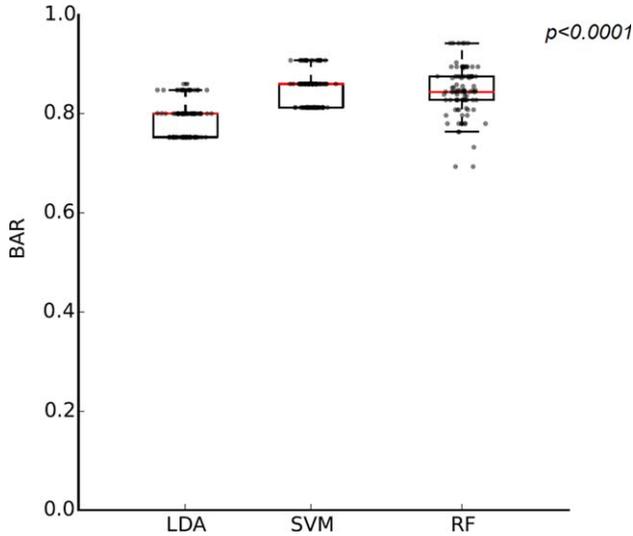
FIG. 5. Comparison of the three learning algorithms balanced accuracy rate. Box plot represents the distribution of BAR obtained from 100 runs of oversampling.

However, EP F-measure and G-mean varied amongst the three methods with SVM having the highest values. This finding demonstrates SVM's better ability in balancing the classification performance between the three groups in comparison to the other two methods.

For PA, SVM, and LDA achieved the highest accuracy (F-measure = 0.9, PA accuracy = 0.95). For the MB group, both SVM and RF had highest number of correctly classified cases (F-measure = 0.9, MB accuracy = 0.88). The misclassification spread across different tumor types, data sites, and scanner types is summarized in Table 4.

The 3D scatter plot in Figure 6 represents LDA and SVM estimated regions. SVM provided improved estimated class boundaries for the three tumor groups that resulted in less overlap between clustered data points and estimated regions from dissimilar tumor types. This difference is more apparent in MB where three cases assigned incorrectly by LDA were correctly classified by SVM.

DISCUSSION

This is the first multi-center study investigating 3T MRS and pattern classification for pediatric tumors. Data represented here are from four different centers collected from 3T scanners at short echo time from three common types of childhood tumors.

Mean metabolite concentrations were shown to differ between tumor types with some individual metabolites differing significantly (Mann-Whitney U test $P < 0.05$) between specific pairs of tumors. The metabolites identified to be significantly different between the three tumor types at 3T in this study generally agrees with previously reported metabolites for the same tumors at 1.5T (6).

Table 4
Summary of the Misclassification Spread across Different Tumor Types, Data Sites, and Scanner Types.

| Tumor type	Ependymoma	Medulloblastoma	Pilocytic astrocytoma
Misclassified cases (n)	1	3–5	1–2
Site of misclassified cases	Alder Hey Children's Hospital (Liverpool)	Birmingham Children's Hospital The Great North Children's Hospital (Newcastle) Alder Hey Children's Hospital (Liverpool)	Birmingham Children's Hospital Alder Hey Children's Hospital (Liverpool) Nottingham Children's Hospital
Scanner manufacturer	Philips	Philips, Siemens	Philips
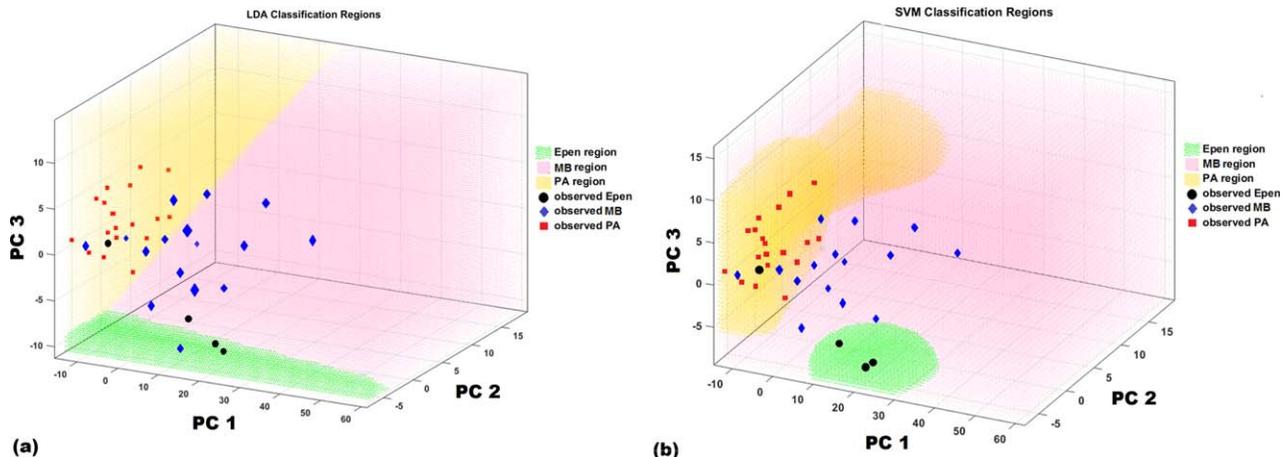
FIG. 6. Three-dimensional scatter plot shows the data clustering for the different tumor types with (**a**) LDA and (**b**) SVM decision boundaries. The graph is oriented so that each clustering can be seen form the best angle with a clear boundary.

Exceptions are metabolites such as Glc, Glu, tLM09, and tLM20 that were reported to be significantly different at 1.5T, and Lac that was found to be significantly different at 3T.

For the 3T data set under study, tCho was higher ($P = 0.01$) in MB compared to PA in agreement with tCho as an indicator of cell proliferation and tumor malignancy (18). EP and MB had higher concentrations of lipids and macromolecules compared with PA that is associated with hypoxia, apoptosis, and necrosis and linked to high malignancy and poor survival (3,19). Tau concentration was significantly higher in MB than PA ($P = 0.0001$) and EP ($P = 0.001$) (20,21). Similarly mIns concentration was significantly higher in EP than MB and PA ($P = 0.05$).

Glc and Glu were not significantly different between the three tumor types as reported in pervious 1.5T studies, but Lac was significantly different between PA and MB ($P = 0.05$). This finding can be because of difference in sample size or increased resolution at 3T allowing more accurate quantitation.

Applying pattern recognition techniques to the metabolite profile data, a maximum balanced accuracy of 86% was achieved for discriminating between astrocytoma, ependymoma, and medulloblastoma. High classification rates are seen despite the relatively small number of cases used to train the classifiers and the inclusion of data from more than one scanner type. The achieved accuracy was better than the reported BAR obtained from short time echo 1.5T data from ten different international centers where similar tumor types and similar data skewness were studied (6). Using LDA for classification, Vicente et al. (6) reported a BAR of 0.79 for tumors from all regions of the brain. However, the reported 1.5T BAR for LDA is in a very close agreement with LDA accuracy when 3T data is used (3T LDA BAR = 0.81).

The discrimination power of the pattern recognition techniques in classifying the ependymoma group alone was on average 75%. This is mainly because of the imbalanced nature of the data. Although SMOTE was used to overpopulate the ependymoma group by 100% to correct for this skewness, the data distribution still remained imbalanced because of the small number of tumors in this group.

In comparing the performance of different pattern recognition techniques, SVM was a fast, easily trained, and reliable discriminator with the highest balanced accuracy rate. This method, with medium flexibility, avoids under- or overfitting of the data. SVMs strongly draw on variation methods in their construction and are designed to yield the best estimate of the optimal separating hyperplane (Fig. 6b). SVM outperforms conventional pattern recognition methods especially when the number of training data is small and number of input variables is large. This is because the conventional pattern recognition methods do not have the mechanism to maximize the margins of class boundaries. Therefore, if some mechanism is introduced to maximize the margins, the generalization ability is improved (22).

Future work should focus on optimizing pattern recognition techniques to classify a wider range of tumor types using 3T MRS. Moreover, a separate prospective study based on an independent test set to ascertain the accuracy of non-invasive prognostic biomarkers, especially for the minority class, provided by 3T MRS is required.

In conclusion, this study demonstrates the ability and high diagnostic accuracy of 3T MRS in detecting key differences in the metabolite profiles for the main types of childhood tumors. Classification performance of 3T MRS compares favorably with previously reported multi-center data sets at 1.5T. 3T MRS with automated processing and pattern recognition providing a useful technique for accurate, non-invasive diagnosis and classification of childhood brain tumors and thereby a powerful diagnostic tool for clinical practice.
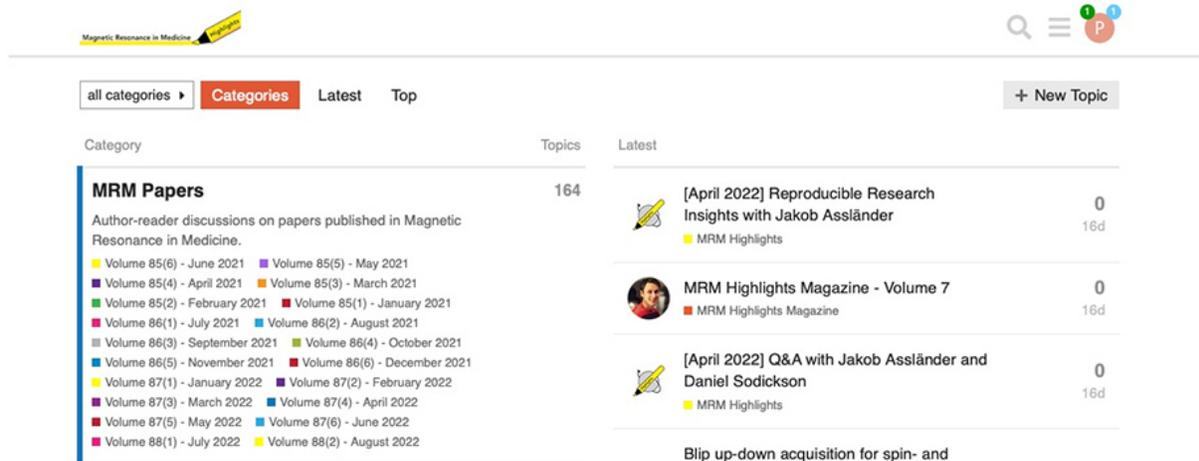
ACKNOWLEDGMENTS

REFERENCES

1. Komori T, Sasaki H, Yoshida K. Revised WHO classification of tumours of the central nervous system:summary of the revision and perspective. No Shinkei Geka 2016;44:625–635.
2. Fetit AE, Novak J, Peet AC, Arvanitits TN. Three-dimensional textural features of conventional MRI improve diagnostic classification of childhood brain tumours. NMR Biomed 2015;28:1174–1184.
3. Panigrahy A, Krieger MD, Gonzalez-Gomez I, Liu X, McComb JG, Finlay JL, Nelson MD Jr, Gilles FH, Bluml S. Quantitative short echo time 1H-MR spectroscopy of untreated pediatric brain tumors: preoperative diagnosis and characterization. AJNR Am J Neuroradiol 2006; 27:560–572.
4. Davison JE, Davies NP, English MW, Philip S, MacPherson LK, Gissen P, Peet AC. Magnetic resonance spectroscopy in the diagnostic evaluation of brainstem lesions in Alexander disease. J Child Neurol 2011;26:356–360.
5. Panigrahy A, Nelson MD Jr, Bluml S. Magnetic resonance spectroscopy in pediatric neuroradiology: clinical and research applications. Pediatr Radiol 2010;40:3–30.
6. Vicente J, Fuster-Garcia E, Tortajada S, et al. Accurate classification of childhood brain tumours by in vivo (1)H MRS - a multi-centre study. Euro J Cancer 2013;49:658–667.
7. Davies NP, Wilson M, Harris LM, Natarajan K, Lateef S, Macpherson L, Sgouros S, Grundy RG, Arvanitis TN, Peet AC. Identification and characterisation of childhood cerebellar tumours by in vivo proton MRS. NMR Biomed 2008;21:908–918.
8. Harris LM, Davies NP, Wilson S, MacPherson L, Natarajan K, English MW, Brundler MA, Arvanitis TN, Grundy RG, Peet AC. Short echo time single voxel 1H magnetic resonance spectroscopy in the diagnosis and characterisation of pineal tumours in children. Pediatr Blood Cancer 2011;57:972–977.
9. Wilson M, Cummins CL, Macpherson L, Sun Y, Natarajan K, Grundy RG, Arvanitis TN, Kauppinen RA, Peet AC. Magnetic resonance spectroscopy metabolite profiles predict survival in paediatric brain tumours. Euro J Cancer 2013;49:457–464.
10. Gonen O, Gruber S, Li BS, Mlynarik V, Moser E. Multivoxel 3D proton spectroscopy in the brain at 1.5 versus 3.0 T: signal-to-noise ratio and resolution comparison. AJNR Am J Neuroradiol 2001;22:1727–1731.
11. Barker PB, Hearshen DO, Boska MD. Single-voxel proton MRS of the human brain at 1.5T and 3.0T. Magn Reson Med 2001;45:765–769.
12. Gruber S, Mlynarik V, Moser E. High-resolution 3D proton spectroscopic imaging of the human brain at 3 T: SNR issues and application for anatomy-matched voxel sizes. Magn Reson Med 2003;49:299–306.
13. Wilson M, Reynolds G, Kauppinen RA, Arvanitis TN, Peet AC. A constrained least-squares approach to the automated quantitation of in vivo (1)H magnetic resonance spectroscopy data. Magn Reson Med 2011;65:1–12.
14. Seymour Z, Panigrahy A, Finlay J, Nelson M, Blüml S. Citrate in pediatric CNS tumors? AJNR Am J Neuroradiol 2008;29:1006–1011.
15. Davies NP, Wilson M, Natarajan K, Sun Y, Macpherson L, Brundler MA, Arvanitis TN, Grundy RG, Peet AC. Non-invasive detection of

glycine as a biomarker of malignancy in childhood brain tumours using in-vivo (1)H MRS at 1.5 Tesla confirmed by ex-vivo high-resolution magic-angle spinning NMR. NMR Biomed 2009;23:80–87.

16. Wilson M, Reynolds G. TARQUIN User Guide Version 4.3.5. 2015. http://tarquin.sourceforge.net/user_guide/tarquin_user_guide.pdf

17. Han H, Wang WY, Mao BH. Borderline-SMOTE: a new over-sampling method in imbalanced data sets learning. In: Huang DS, Zhang XP, Huang GB, editors. Advances in intellegent computing. ICIC 2005. Lecture Notes in Computer Science, vol 3644. Berlin, Heidelberg: Springer; 2005. p 878–887.

18. Imamura K. Proton MR spectroscopy of the brain with a focus on chemical issues. Magn Reson Med Sci 2003;2:117–132.

19. Remy C, Fouilhe N, Barba I, et al. Evidence that mobile lipids detected in rat brain glioma by 1H nuclear magnetic resonance correspond to lipid droplets. Cancer Res 1997;57:407–414.

20. Peet AC, Lateef S, MacPherson L, Natarajan K, Sgouros S, Grundy RG. Short echo time 1 H magnetic resonance spectroscopy of childhood brain tumours. Childs Nerv Syst 2007;23:163–169.

21. Moreno-Torres A, Martinez-Perez I, Baquero M, Campistol J, Capdevila A, Arus C, Pujol J. Taurine detection by proton magnetic resonance spectroscopy in medulloblastoma: contribution to noninvasive differential diagnosis with cerebellar astrocytoma. Neurosurgery 2004;55:824–829.

22. Abe S. Support vector machines for pattern classification. London, New York: Springer; 2010. 471 p.

WOULD YOU LIKE TO POST AN INFORMAL COMMENT ABOUT THIS PAPER, OR ASK THE AUTHORS A QUESTION ABOUT IT?

If so, please visit https://mrm.ismrm.org/ and register for our Magn Reson Med Discourse site (registration is free).

Magn Reson Med is currently listing the top 8 downloaded papers from each issue (including Editor's Picks) for comments and questions on the Discourse web site.

However, we are happy to list this or any other papers (please email mrm@ismrm.org to request the posting of any other papers.)

We encourage informal comment and discussion about Magn Reson Med papers on this site. Please note, however, that a formal errata from the authors should still be submitted in the usual way via our Manuscript Central online submission system.